Numerical implementation of non-local polycrystal plasticity using fast Fourier transforms

Ricardo A. Lebensohn [a,*], Alan Needleman [b]

[a] Materials Science and Technology Division, Los Alamos National Laboratory, MS G755, Los Alamos, NM 87845, USA
[b] Department of Materials Science and Engineering, Texas A&M University, College Station, TX 77843, USA

ARTICLE INFO

ABSTRACT

We present the numerical implementation of a non-local polycrystal plasticity theory using the FFT-based formulation of Suquet and co-workers. Gurtin (2002) non-local formulation, with geometry changes neglected, has been incorporated in the EVP-FFT algorithm of Lebensohn et al. (2012). Numerical procedures for the accurate estimation of higher order derivatives of micromechanical fields, required for feedback into single crystal constitutive relations, are identified and applied. A simple case of a periodic laminate made of two fcc crystals with different plastic properties is first used to assess the soundness and numerical stability of the proposed algorithm and to study the influence of different model parameters on the predictions of the non-local model. Different behaviors at grain boundaries are explored, and the one consistent with the micro-clamped condition gives the most pronounced size effect. The formulation is applied next to 3-D fcc polycrystals, illustrating the possibilities offered by the proposed numerical scheme to analyze the mechanical response of polycrystalline aggregates in three dimensions accounting for size dependence arising from plastic strain gradients with reasonable computing times.

1. Introduction

The dependence of the mechanical response of metal polycrystals on grain size has been known since the work of Hall (1951) and Petch (1953). A variety of theories have been proposed and analyses carried out in an attempt to quantify this effect, e.g. Eshelby et al. (1951); Hirth and Lothe (1968); Ashby (1970); Biner and Morris (2003); Balint et al. (2008); Counts et al. (2008); Cordero et al. (2012); Quek et al. (2014). This body of work has mainly focused on understanding the scaling of overall polycrystal stress–strain response with mean grain size.

Since the main mechanism of metal plasticity is dislocation nucleation and motion, and dislocations are characterized by a length scale given by the Burgers vector, it is not surprising that size dependence emerges. In particular, plastic strain gradients give rise to dislocation structures, termed geometrically necessary dislocations (GNDs) that induce a size effect at the micro scale (Nye, 1953; Ashby, 1970). Experimental observation of size dependence at the micro scale in torsion (Fleck et al., 1994), indentation (Guzman et al., 1993; Ma and Clarke, 1995) and bending (Stölken and Evans, 1998) inspired the development of a wide variety of theories of plasticity that incorporate a size effect arising from the presence of plastic

ARTICLE IN PRESS

2   *R.A. Lebensohn, A. Needleman / J. Mech. Phys. Solids ▪ (▪▪▪▪) ▪▪▪–▪▪▪*

strain gradients, including, for example, those discussed in Fleck and Hutchinson (1993, 1997, 2001); Gao et al. (1999); Acharya and Bassani (2000); Gurtin (2000, 2002); Hwang et al. (2004); Kuroda and Tvergaard (2008); Kuroda (2015). The experiments of Uchic et al. (2004) and Greer et al. (2005) on the size dependent response of micron scale pillars subject to uniaxial compression highlighted the fact that dislocation-based size effects do arise from mechanisms other than plastic strain gradients.

Developing a capability for predicting the dependence of the mechanical response of polycrystals on grain size is a computationally challenging task. It is to be expected, for example, that the mechanical response will depend on the grain size distribution, not just the mean grain size, and, perhaps in addition, even on the specific orientation of neighboring grains in a polycrystal. In particular, these details of the grain orientation distribution are expected to be of importance in understanding the stress states in grains and near grain boundaries that promote various failure mechanisms. Hence, there is a need for a computationally efficient framework to calculate the mechanical response of polycrystals accounting for size effects in order that numerical studies needed to quantify these effects can be carried out.

One approach, as in Biner and Morris (2003), Balint et al. (2008), Quek et al. (2014), is to use discrete dislocation plasticity which can account for all dislocation-based size effects. However, carrying out parameter studies, in three dimensions, of statistically representative polycrystals using discrete dislocation plasticity is well beyond current computational capabilities. Another approach, pursued here, is to base the calculations on a phenomenological size-dependent crystal plasticity theory. A variety of size dependent crystal plasticity theories have been proposed, e.g. Gurtin (2000, 2002); Forest (2008); Kuroda and Tvergaard (2008), and a comparison of several size dependent crystal plasticity theoretical frameworks has been presented by Mayeur and McDowell (2014). Here, our calculations are based on the crystal plasticity theory introduced by Gurtin (2000, 2002) that is, at present, the most widely employed such theory. This theory accounts for size dependence arising from plastic strain gradients and, as a consequence, involves slip gradients and higher order boundary conditions. These complicate crystal plasticity (CP) finite element (FE) calculations, which have been generally restricted to two-dimensional problems and single crystals with two or three slip systems (e.g. Bittencourt et al., 2003; Bittencourt, 2014; Niordson and Kysar, 2014).

In recent years, a highly efficient alternative to CPFE for the numerical treatment of plasticity of heterogeneous media using fast Fourier transforms (FFT) has been proposed and applied to a suite of problems involving the determination of micromechanical fields and effective response in polycrystalline materials. This spectral formulation, originally developed by Suquet and co-workers (Moulinec and Suquet, 1994, 1998; Michel et al., 2000, 2001) as an efficient method to compute the micromechanical response of periodic heterogeneous materials, including the possible use of direct input from microstructural images, has been adapted to polycrystals deforming in the relatively simple thermo-elastic (Brenner et al., 2009; Anglin et al., 2014) and rigid-viscoplastic (Lebensohn, 2001; Lebensohn et al., 2008, 2009) regimes, and recently extended to polycrystalline aggregates deforming in the elasto-viscoplastic (EVP) regime (Lebensohn et al., 2012; Grennerat et al., 2012; Eisenlohr et al., 2013). In these EVP-FFT implementations, a local formulation of crystal plasticity was adopted, rendering their predictions size-independent. While the potential for an efficient non-local plasticity FFT-based implementation has been recognized, overcoming the numerical challenges associated with the required computation and use in the constitutive relation of higher order derivatives of the plastic distortion field was only possible considering the alternative use of discrete Fourier transforms (DFT) (Müller, 1998; Dreyer et al., 1999; Willot and Pellegrini, 2008; Willot, 2015) in lieu of the original Moulinec-Suquet continuous Fourier transform (CFT)-based algorithm, in particular drawing upon recent work by Berbenni et al. (2014) devoted to the calculation of stress fields associated to the presence of disclinations in elastic media using the FFT-based approach.

Here, we present an FFT-based method for analyzing 3-D polycrystals accounting for size dependence arising from slip gradients. In this initial study, geometry changes are neglected. The plan of this paper is as follows. In Section 2 we present the salient aspects of Gurtin (2002) non-local plasticity theory. In Section 3 we cast the latter into the elastic-viscoplastic FFT algorithm of Lebensohn et al. (2012), including the computation of a back-stress field that in Gurtin (2002) theory affects the constitutive behavior at the single crystal level. Next, in Section 3, important numerical details of the non-local elastic-viscoplastic FFT implementation are provided. In Section 4 we apply our formulation to a simple bicrystal laminate configuration in order to demonstrate the numerical stability of the method and to study the influence of various model parameters and interface conditions on the prediction of size dependence. We also consider the case of 3-D polycrystals. We consider two types of boundary conditions at grain boundaries: (i) one corresponding to allowing slip to freely pass through the boundary and (ii) one completely blocking slip. As discussed for example by Danas et al. (2012) and by Quek et al. (2014), the actual behavior of grain boundaries is more complex and is expected to fall between these regimes. Within the theoretical framework used in our analyses, Gurtin and Needleman (2005) have developed interface boundary conditions for the non-local framework used in the calculations here that can model behavior between these two regimes. However, our initial results using the limiting cases do illustrate the capabilities and efficiency of the proposed FFT implementation. Section 5 contains some additional remarks and in Section 6 we draw our conclusions.

2. Non-local plasticity formulation

We consider a periodic unit cell consisting of a specified number of fcc crystal grains subject to a prescribed overall stress/deformation state. Geometry changes are neglected. The constitutive response of each grain is taken to be

ARTICLE IN PRESS

R.A. Lebensohn, A. Needleman / J. Mech. Phys. Solids ∎ (∎∎∎∎) ∎∎∎–∎∎∎   3

characterized by the non-local theory of crystal plasticity due to Gurtin (2000, 2002) specialized to circumstances where geometry changes are negligible. The governing equations, as implemented in our analyses, are briefly presented here. A more complete description and additional references can be found in Gurtin (2000, 2002) and Bittencourt et al. (2003).

The total displacement gradient $u_{i,j}$ is written as the sum of elastic and plastic parts so that

$$u_{i,j} = u_{ij}^e + u_{ij}^p \tag{1}$$

The plastic distortion part is given by

$$u_{ij}^p = \sum_\beta \gamma^{(\beta)} \mu_{ij}^{(\beta)} \tag{2}$$

where the (non-symmetrized) Schmid tensor is defined as

$$\mu_{ij}^{(\beta)} = s_i^{(\beta)} m_j^{(\beta)} \tag{3}$$

with $\beta = 1, 2, \ldots N$, where N is the number the number of slip systems, $s_i^{(\beta)}$ is the slip direction, $m_j^{(\beta)}$ is the slip plane normal and $\gamma^{(\beta)}$ is the accumulated slip on slip system β. The resolved shear stress on system β is given in terms of the stress σ_{ij} by

$$\tau^{(\beta)} = \mu_{ij}^{(\beta)} \sigma_{ij} \tag{4}$$

With body forces neglected, the principle of virtual work can be written as

$$\int_V \left[\sigma_{ij} \delta \varepsilon_{ij} + \sum_\beta \left(\pi^{(\beta)} - \tau^{(\beta)} \right) \delta \gamma^{(\beta)} + \sum_\beta \xi_i^{(\beta)} \delta \gamma_{,i}^{(\beta)} \right] dV = \int_S \sum_\beta q^{(\beta)} \delta \gamma^{(\beta)} dS + \int_S t_i \delta u_i dS \tag{5}$$

where $\pi^{(\beta)}$ and $\xi_i^{(\beta)}$ are work-conjugates to the slip and slip gradients and $q^{(\beta)} = \xi_i^{(\beta)} n_i$ and $t_i = \sigma_{ij} n_j$.

From Eq. (5) the governing equations are

$$\sigma_{ij,j} = 0 \tag{6}$$

and

$$\pi^{(\beta)} - \tau^{(\beta)} - \xi_{i,i}^{(\beta)} = 0 \tag{7}$$

with the boundary conditions being that u_i and $\gamma^{(\beta)}$ satisfy periodicity on S and that the average stress state is consistent with the state prescribed. Additional boundaries conditions at grain boundaries analyzed here are the so-called micro-free boundary condition, $q^{(\beta)} = 0$, and micro-clamped boundary condition, $\gamma^{(\beta)} = 0$.

The stress-strain relation at time $(t + \Delta t)$ is written as

$$\sigma_{ij} = L_{ijkl} \left[\varepsilon_{kl} - sym \left(u_{kl}^{p,t} \right) - \sum_\beta \dot{\gamma}^{(\beta)} sym \left(\mu_{kl}^{(\beta)} \right) \Delta t \right] \tag{8}$$

where L_{ijkl} is the tensor of elastic moduli, $sym(\ )$ denotes the symmetric part of a second order tensor and a superposed dot denotes differentiation with respect to time. The superscript t indicates the corresponding field value at time t. All other fields are evaluated at $(t + \Delta t)$, in which case the time superscripts are omitted for simplicity.

The micro-stress $\xi_r^{(\beta)}$ is taken to be linearly related to the Nye tensor α_{ij}, calculated as

$$\alpha_{ij} = e_{jpq} u_{iq,p}^p \tag{9}$$

to give

$$\xi_r^{(\beta)} = \ell^2 \pi_0 \ e_{rsi} \ e_{ipq} \mu_{ms}^{(\beta)} u_{mq,p}^p \tag{10}$$

where e_{ijk} is the permutation tensor and ℓ and π_0 are material parameters that have dimensions of length and stress, respectively.

The gradient of the micro-stress, i.e. the micro-force, which is the quantity entering in Eq. (7), is

$$\xi_{r,r}^{(\beta)} = \ell^2 \pi_0 \ e_{rsi} e_{ipq} \left(\mu_{ms}^{(\beta)} u_{mq,pr}^p + \mu_{ms,r}^{(\beta)} u_{mq,p}^p \right) \tag{11}$$

and its rate is given by

$$\dot{\xi}_{r,r}^{(\beta)} = \ell^2 \pi_0 \ e_{rsi} e_{ipq} \left(\mu_{ms}^{(\beta)} \dot{u}_{mq,pr}^p + \mu_{ms,r}^{(\beta)} \dot{u}_{mq,p}^p \right) \tag{12}$$

The plastic response is taken to be rate-dependent with the slip rate on each system given by

ARTICLE IN PRESS

4   R.A. Lebensohn, A. Needleman / J. Mech. Phys. Solids ∎ (∎∎∎∎) ∎∎∎–∎∎∎

$$\dot{\gamma}^{(\beta)} = \dot{\gamma}_0 \left[\frac{\pi^{(\beta)}}{g^{(\beta)}} \right] \left[\frac{|\pi^{(\beta)}|}{g^{(\beta)}} \right]^{(n-1)} = \dot{\gamma}_0 \left[\frac{\tau^{(\beta)} + \xi_{r,r}^{(\beta)}}{g^{(\beta)}} \right] \left[\frac{|\tau^{(\beta)} + \xi_{r,r}^{(\beta)}|}{g^{(\beta)}} \right]^{(n-1)} \tag{13}$$

with $\dot{\gamma}_0$ a reference strain rate, and n the stress exponent, inverse of strain rate sensitivity. In Eq. (13) the negative of the gradient of the micro-stress, $-\xi_{r,r}^{(\beta)}$, acts as a back-stress.

The flow strength $g^{(\beta)}$ has the initial value π_0 for all slip systems and evolves as:

$$\dot{g}^{(\beta)} = \sum_{\alpha} h^{(\alpha\beta)} |\dot{\gamma}^{(\beta)}| \tag{14}$$

Here we adopt a simple hardening law, i.e. linear, and with no difference between self and latent hardening coefficients: $h^{(\alpha\beta)} = H_0$, $\forall \, \alpha, \beta$, such that

$$\dot{g}^{(\beta)} = H_0 \sum_{\alpha} |\dot{\gamma}^{(\beta)}| \tag{15}$$

(Eqs. (15) and 12) provide the hardening rates, dependent on the slip rates and their derivatives, respectively, affecting the slip-level flow condition (Eq. 13), corresponding to the dissipative and energetic hardening terms, respectively. As in a variety of previous analyses based on Gurtin (2002) crystal plasticity framework, e.g. Bittencourt et al. (2003), Bittencourt (2014), the effect of GNDs is only incorporated in the energetic hardening term, (Eqs. (10)–12). The presumption in this is that the main contribution to the dissipative hardening in Eq. (15) comes from the statistical dislocations. In principle, the effect of GNDs can be incorporated into the dissipative hardening, as for example in Niordson and Kysar (2014). Inclusion of such terms involves no additional computational complexity but does introduce additional parameters. Since our focus is on the computational formulation, we only include the effect of GNDs in the energetic hardening term in the calculations presented here.

3. Numerical implementation

3.1. Elasto-viscoplastic FFT-based method

A thorough description of the small strain EVP-FFT formulation is presented in Lebensohn et al. (2012). Here the procedure will be outlined with a focus on those aspects relevant to the non-local formulation.

An initially cubic, periodic unit cell is chosen with side length h. A uniform grid { $\mathbf{x}^d$} of $N_1 \times N_2 \times N_3$ points is specified, with position vector given by $\mathbf{x}^d = ((i - 1) \times h/N_1, (j - 1) \times h/N_2, (k - 1) \times h/N_3)$, with $i = 1, N_1$, $j = 1, N_2$, $k = 1, N_3$. Known field quantities, such as material properties, crystal orientations, etc., are assigned values, while unknown field quantities, like displacements, strains, stresses, slips, etc., are calculated at these points.

A position-independent stiffness tensor L^0 is chosen and the stress–strain relation, Eq. (8), is re-written as

$$\sigma_{ij}(\mathbf{x}) = L_{ijkl}^0 \varepsilon_{kl}(\mathbf{x}) + \varphi_{ij}(\mathbf{x}) \tag{16}$$

where $(\mathbf{x})$ explicitly identifies position-dependent quantities. According to Eq. (8), the polarization field is given by

$$\varphi_{ij}(\mathbf{x}) = \Delta L_{ijkl}(\mathbf{x}) \left[\varepsilon_{kl}(\mathbf{x}) - sym\left(u_{kl}^{p,t}(\mathbf{x}) \right) - \sum_{\beta} \dot{\gamma}^{(\beta)}(\mathbf{x}) \; sym\left(\mu_{kl}^{(\beta)}(\mathbf{x}) \right) \; \Delta t \right] \tag{17}$$

where $\Delta L(\mathbf{x}) = L(\mathbf{x}) - L^0$. The macro-stress equilibrium condition, Eq. (6), then becomes

$$L_{ijkl}^0 u_{k,lj}(\mathbf{x}) + \varphi_{ij,j}(\mathbf{x}) = 0 \tag{18}$$

The choice of L^0 does not modify the final result of the computation of micromechanical fields but does affect the convergence of the iterative procedure described subsequently. In the present implementation, L^0 is taken to be the Voigt average tensor of the local elastic moduli, i.e. $L_{ijkl}^0 = \langle L_{ijkl}(\mathbf{x}) \rangle$, where $\langle \cdot \rangle$ indicates average of field quantities over the periodic volume element.

The boundary condition on the displacement field, in addition to periodicity, is that the spatial average of the stress field corresponds to a prescribed state that in all cases here is uniaxial tension, $\langle \sigma_{11}(\mathbf{x}) \rangle = \Sigma_{11}$, with all other $\langle \sigma_{ij}(\mathbf{x}) \rangle = 0$. The only boundary condition directly imposed on $u_{ij}^p(\mathbf{x})$ through the micro-relations (Eqs. (7) and 11) is periodicity.

To solve Eq. (18), let us consider the Green's function $G_{km}(\mathbf{x} - \mathbf{x}')$ associated with the displacement field $u_k(\mathbf{x})$ that satisfies

$$L_{ijkl}^0 G_{km,lj}(\mathbf{x} - \mathbf{x}') + \delta_{im} \, \delta(\mathbf{x} - \mathbf{x}') = 0 \tag{19}$$

After some manipulation (see Lebensohn et al., 2012), the displacement and displacement gradient fields are obtained from convolution integrals:

ARTICLE IN PRESS

R.A. Lebensohn, A. Needleman / J. Mech. Phys. Solids ▮ (▮▮▮▮) ▮▮▮–▮▮▮ 5

$$u_k(\mathbf{x}) = \int_{R^3} G_{ki,j}(\mathbf{x} - \mathbf{x}') \; \varphi_{ij}(\mathbf{x}') \; d\mathbf{x}' \tag{20}$$

$$u_{k,l}(\mathbf{x}) = \int_{R^3} G_{ki,jl}(\mathbf{x} - \mathbf{x}') \; \varphi_{ij}(\mathbf{x}') \; d\mathbf{x}' \tag{21}$$

For convenience, the above convolutions are computed in Fourier space. For example, from Eq. (21), the strain field is calculated as

$$\varepsilon_{ij}(\mathbf{x}) = E_{ij} + FT^{-1} \left\{ sym \left(\hat{\Gamma}^0_{ijkl}(\mathbf{k}) \right) \hat{\varphi}_{kl}(\mathbf{k}) \right\} (\mathbf{x}) \tag{22}$$

where the hat symbol indicates Fourier transform (FT), $\mathbf{k}$ is a point (frequency) of Fourier space, and E_{ij} is the strain pre-scribed on the unit cell. The Green operator in Fourier space, which is only a function of the reference stiffness tensor and the frequency, is given by

$$\hat{\Gamma}^o_{ijkl}(\mathbf{k}) = - k_j k_l \hat{G}_{ik}(\mathbf{k}) \text{ with } \hat{G}_{ik}(\mathbf{k}) = \left[L^o_{kjil} \; k_l k_j \right]^{-1} \tag{23}$$

Numerically, the above fields in Fourier space are evaluated on a grid $\{\mathbf{k}^d\}$ of the same size $(N_1 \times N_2 \times N_3)$ as the grid in Cartesian space.

If the polarization field $\varphi_{ij}(\mathbf{x})$ were known, then the above expressions would directly give the displacement and strain fields. At each time step, the procedure uses an initial guess for $\varphi_{ij}(\mathbf{x})$ to calculate $\varepsilon_{ij}(\mathbf{x})$ according to Eq. (22), then the stress field $\sigma_{ij}(\mathbf{x})$ and the slip rate fields $\dot{\gamma}^{(\beta)}(\mathbf{x})$ are updated solving algebraic systems of non-linear equations given by Eq. (8) combined with (Eqs. (4) and 13). With these re-evaluated fields, the polarization is updated using Eq. (17) and the procedure is repeated until convergence in this polarization loop is attained with a specified tolerance.

### 3.2. Numerical details of the non-local theory implementation

In the non-local theory, a key step is the evaluation of $-\xi^{(\beta)}_{r,r}$ for use in Eq. (13) as part of the iterative procedure described above. In particular, (Eqs. (11) and 12) contain spatial derivatives of the Schmid tensor field $\mu^{(\beta)}_{js,r}(\mathbf{x})$. In a small deformation framework, and for an initially fully-recrystallized polycrystal, the values of $\mu^{(\beta)}_{js}$ can be considered constant in each grain, so that in the interior of each grain those spatial derivatives vanish. However, the Schmid tensor values vary, in general, from grain to grain, i.e. across grain boundaries. If the contribution to the back-stress of the term involving those derivatives is neglected, the rate at which the back-stress varies can be approximated by

$$-\dot{\xi}^{(\beta)}_{r,r}(\mathbf{x}) = - \ell^2 \pi_0 \; e_{rsi} e_{ipq} \mu^{(\beta)}_{ms}(\mathbf{x}) \; FT^{-1} \left[\hat{\dot{u}}^p_{mq,pr}(\mathbf{k}) \right] (\mathbf{x}) \tag{24}$$

This approximation amounts to consider the presence of ideally aligned slip systems in neighbor grains providing perfect slip transmission across grain boundaries. This assumption is valid only in some ideal cases, as in most of the bicrystal configurations studied in Section 4.1, but, in general, the assumption of ideal transmissibility across grain boundaries un-derestimates the non-local effects, rendering the predictions a lower-bound estimate of these effects, as in the polycrystal cases studied in Section 4.2.
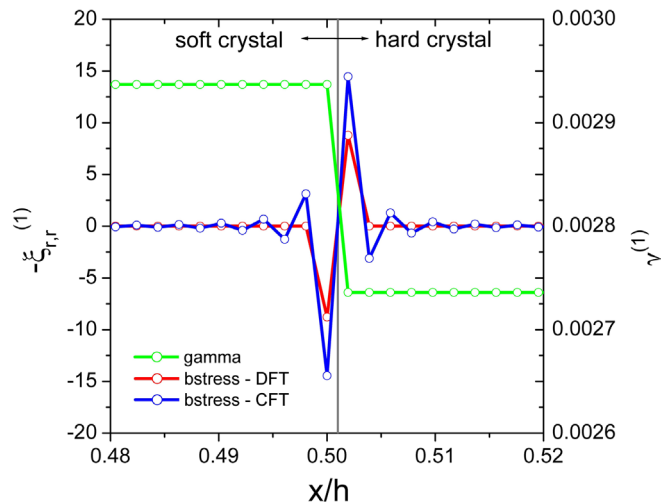
Fig. 1. Zoom near the interface at $x = h/2$ of the slip field and back-stress fields calculated with DFT and CFT, for active slip system #1 after 1% strain, predicted by the local EVP-FFT formulation. Symbols indicate the position of the Fourier points at which the fields are evaluated.

ARTICLE IN PRESS

6   R.A. Lebensohn, A. Needleman / J. Mech. Phys. Solids ∎ (∎∎∎∎) ∎∎∎–∎∎∎
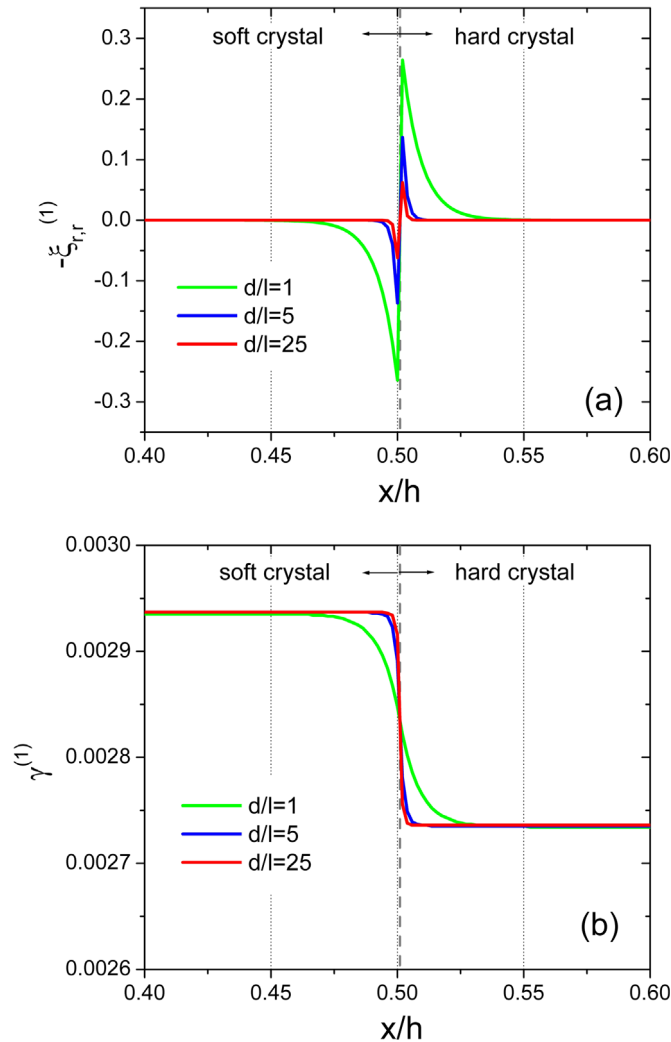
Fig. 2. Influence of the material length-scale. Zoom near the interface of (a) back-stress and (b) slip fields, for active slip system #1 after 1% strain, for different d/ℓ ratios.

If the Schmid tensor jumps across grain boundaries are considered, the back-stress is given by

$$-\dot{\xi}_{r,r}^{(\beta)}(\mathbf{x}) = -\ell^2 \pi_0 \; e_{rsi} e_{ipq} \; FT^{-1}\left\{ \left\{ FT \left\{ \mu_{ms}^{(\beta)}(\mathbf{x}) \; FT^{-1}\left\{ \hat{\dot{u}}_{mq,p}^{p}(\mathbf{k}) \right\}(\mathbf{x}) \right\}, r \right\}(\mathbf{k}) \right\}(\mathbf{x}) \tag{25}$$

Note that in writing (Eqs. (24), 25), the mean value of the micro-force field is assumed to vanish, consistent with its internal field status. In Section 4.1 we present a comparison between the predictions obtained with the approximation given by Eq. (24) and the consideration of Schmid tensor jumps by means of Eq. (25), in the case of a bicrystal with lattice misorientation between crystals.

A crucial aspect of the present numerical implementation is the accurate determination of the partial derivatives of the plastic distortion appearing in the expressions of the back-stress field. As shown in (Eqs. (24), 25), these derivatives are calculated in Fourier space and then anti-transformed. For that purpose, after the determination of the slip rate fields $\dot{\gamma}^{(\beta)}(\mathbf{x})$, $\dot{u}_{ij}^{p}(\mathbf{x})$ is obtained using the rate form of Eq. (2). The required partial derivatives of the plastic distortion rate field in Fourier space are then calculated using the expressions provided by Berbenni et al. (2014) based on earlier work by Müller (1998) and Dreyer at al. (1999), in which derivatives are calculated by means of corresponding central finite difference expressions, to which discrete Fourier transforms are taken and the shift theorem is applied (see Berbenni et al. (2014) for details). In the case of the approximation given by Eq. (24), the resulting expression for $\hat{\dot{u}}_{mq,kr}^{p}(i, j, k)$, where $i = 1, N_1; \; j = 1, N_2; \; k = 1, N_3$ indicate the coordinate in the grid in Fourier space, is

ARTICLE IN PRESS

R.A. Lebensohn, A. Needleman / J. Mech. Phys. Solids ∎ (∎∎∎∎) ∎∎∎–∎∎∎　　　　　　7
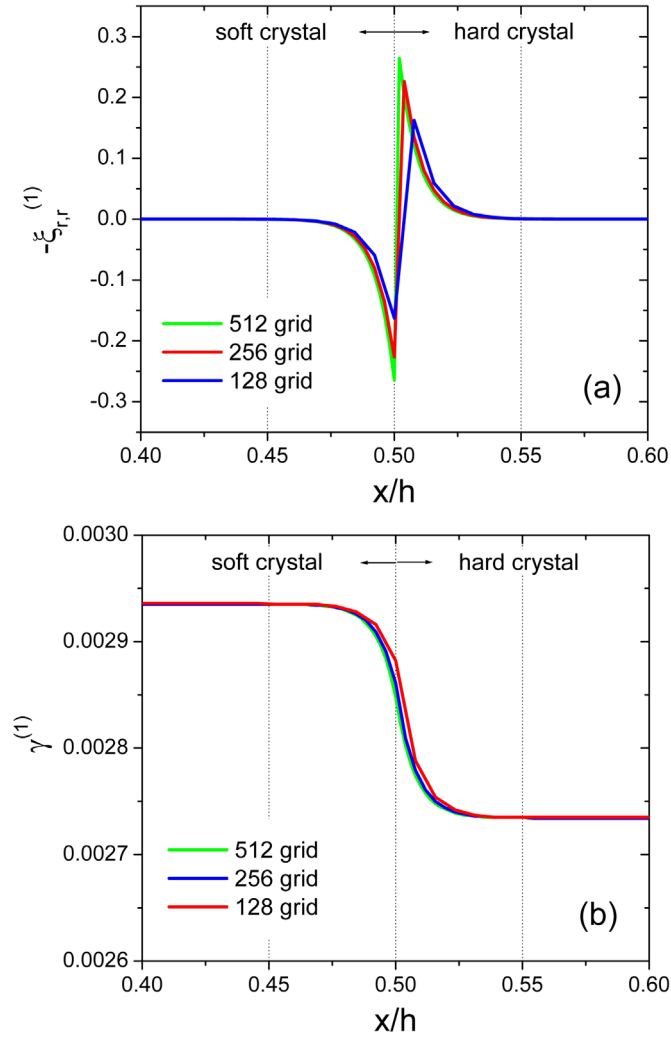
Fig. 3. Influence of the FFT discretization. Zoom near the interface of (a) back-stress and (b) slip fields, for active slip system #1 after 1% strain, for $d/\ell = 1$ and different discretizations.

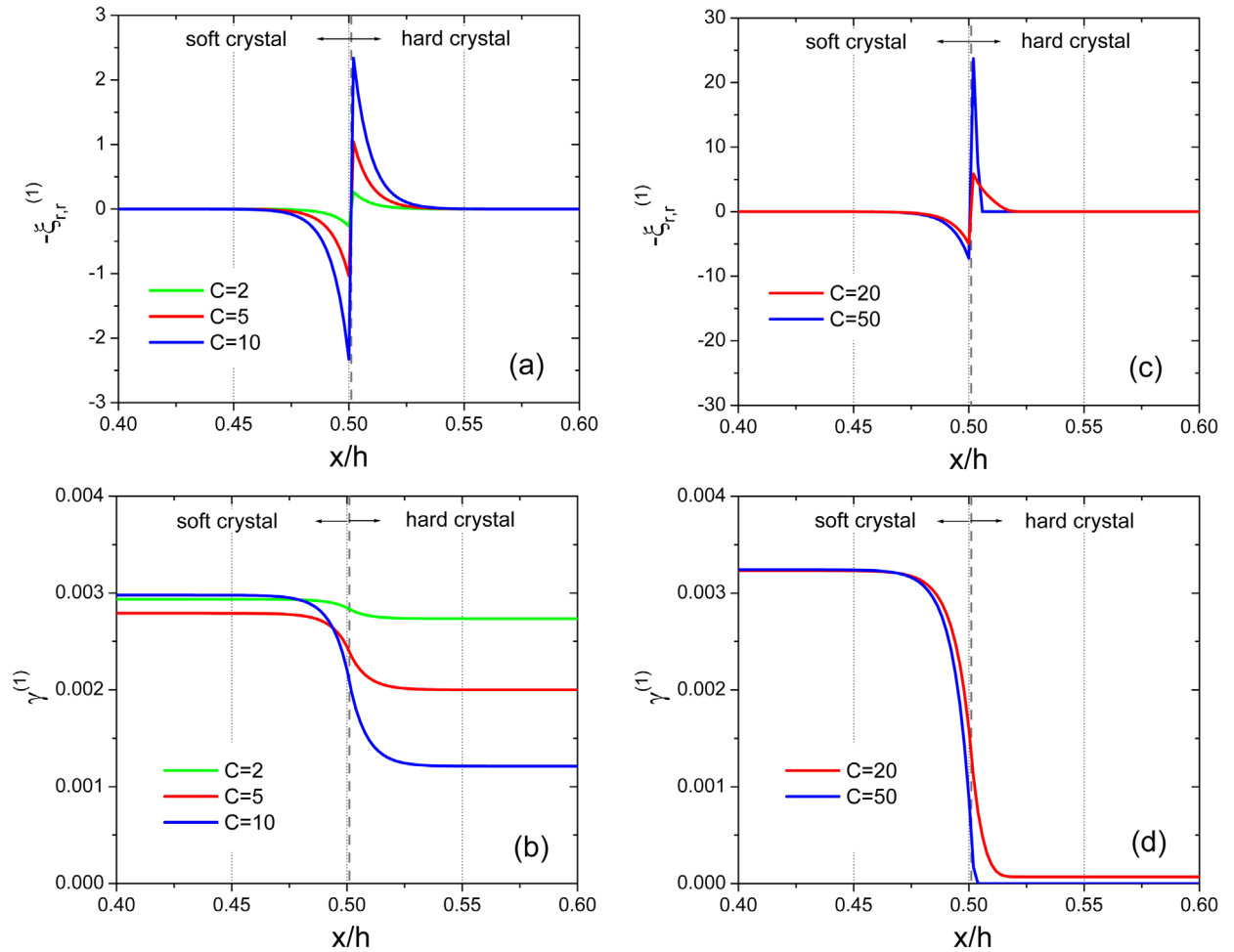$$\hat{u}^{p}_{mq,kr}(i, j, k) = \hat{u}^{p}_{mq}(i, j, k) \times D^{II,DFT}_{kr}(i, j, k) \tag{26}$$

where

$$D^{II,DFT}_{kr}(i, j, k) =$$

$$\begin{vmatrix} \dfrac{2}{N_1^2}\left(\cos\left(\dfrac{2\pi(i-1)}{N_1}\right) - 1\right) & sym & sym \\[2ex] \dfrac{1}{2N_1N_2}[\cos(2\pi(i-1)/N_1 + 2\pi(j-1)/N_2) - & \dfrac{2}{N_2^2}\left(\cos\left(\dfrac{2\pi(j-1)}{N_2}\right) - 1\right) & sym \\ \cos(2\pi(i-1)/N_1 - 2\pi(j-1)/N_2)] & & \\[2ex] \dfrac{1}{2N_1N_3}[\cos(2\pi(i-1)/N_1 + 2\pi(k-1)/N_3) - & \dfrac{1}{2N_2N_3}[\cos(2\pi(j-1)/N_2 + 2\pi(k-1)/N_3) - & \dfrac{2}{N_3^2}\left(\cos\left(\dfrac{2\pi(k-1)}{N_3}\right) - 1\right) \\ \cos(2\pi(i-1)/N_1 - 2\pi(k-1)/N_3)] & \cos(2\pi(j-1)/N_2 - 2\pi(k-1)/N_3)] & \end{vmatrix} \tag{27}$$

(Eqs. (26), 27) are the preferred alternative to calculate second derivatives, instead of the use continuous Fourier transforms prior to discretization that results in

$$\hat{u}^{p}_{mq,kr}(i, j, k) = \hat{u}^{p}_{mq}(i, j, k) \times D^{II,CFT}_{kr}(i, j, k) \tag{28}$$

where

ARTICLE IN PRESS

8   R.A. Lebensohn, A. Needleman / J. Mech. Phys. Solids ∎ (∎∎∎∎) ∎∎∎–∎∎∎

Fig. 4. Influence of the contrast between plastic properties of the crystals. (a,c) Back-stress and (b,d) slip fields in the region near the interface, for active slip system #1 after 1% strain, for $d/\ell = 1$ and different contrasts between plastic flow strengths.

$$D_{kr}^{II,CFT}(i, j, k) =$$

$$
\begin{vmatrix}
-4\pi \left(\dfrac{(i-1) - \alpha^i N_1}{N_1} \right)^2 & sym & sym \\[2em]
-4\pi \dfrac{\left((i-1) - \alpha^i N_1 \right) \times \left((j-1) - \alpha^j N_2 \right)}{N_1 N_2} & -4\pi \left(\dfrac{(j-1) - \alpha^j N_2}{N_2} \right)^2 & sym \\[2em]
-4\pi \dfrac{\left((i-1) - \alpha^i N_1 \right) \times \left((k-1) - \alpha^k N_3 \right)}{N_1 N_3} & -4\pi \dfrac{\left((j-1) - \alpha^j N_2 \right) \times \left((k-1) - \alpha^k N_3 \right)}{N_2 N_3} & -4\pi \left(\dfrac{(k-1) - \alpha^k N_3}{N_3} \right)^2
\end{vmatrix}
\tag{29}
$$

with

$$
\alpha^h = \begin{vmatrix} 0 & if \ \ h \le N_h/2 \\ 1 & if \ \ h > N_h/2 \end{vmatrix} for \ \ h = i, j, k
\tag{30}
$$

In the case of Eq. (25), first derivatives, e.g. $\hat{\dot{u}}_{mq,p}^{p}$, are calculated as
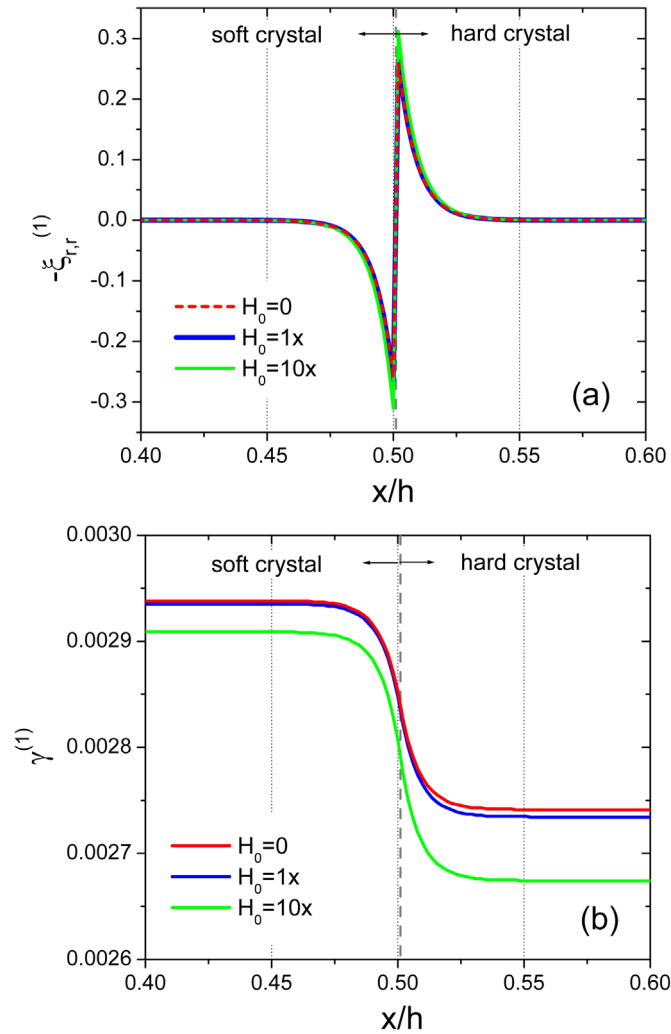
$$
\hat{\dot{u}}_{mq,p}^{p}(i, j, k) = \hat{\dot{u}}_{mq}^{p}(i, j, k) \times D_p^{I,DFT}(i, j, k)
\tag{31}
$$

with

$$
D_p^{I,DFT}(i, j, k) = \left(\frac{-i}{N_1} \sin\left(\frac{2\pi(i-1)}{N_1} \right), \ \frac{-i}{N_2} \sin\left(\frac{2\pi(j-1)}{N_2} \right), \ \frac{-i}{N_3} \sin\left(\frac{2\pi(k-1)}{N_3} \right) \right)
\tag{32}
$$

where the symbol i appearing in the numerators of the leading factors is the imaginary unit, and the negative sign affecting i

ARTICLE IN PRESS

R.A. Lebensohn, A. Needleman / J. Mech. Phys. Solids ∎ (∎∎∎∎) ∎∎∎–∎∎∎ 9

Fig. 5. Influence of dissipative hardening. (a) Back-stress and (b) slip fields in the region near the interface, for active slip system #1 after 1% strain, for $d/\ell = 1$ and different values of the dissipative hardening parameter H_0.

corresponds to the convention of a positive exponent in the direct Fourier transform.

As pointed out by Berbenni et al. (2014) in the context of another application of the FFT-based approach to calculate stress fields associated to the presence of disclinations in elastic media, also requiring the evaluation of higher order derivatives of incompatible distortion fields, the use of the DFT expressions (e.g. (Eqs. (26), 27)), as alternative to the standard CFT expressions of such higher order derivatives (e.g. (Eqs. (28)–30)), results in smooth fields without Gibbs oscillations. This improved estimation of the back-stress field is critical, given that the latter enters directly into the non-linear constitutive relation (Eq. (13)), making any spurious oscillation strongly detrimental to the numerical stability of the proposed method. A comparison between the use of DFT and CFT to calculate back-stresses is given in next section.

Another important aspect of the present implementation is the adopted time integration of the hardening parameters, whose evolution is given by Eq. (15) and Eqs. (24) or (25), for the dissipative and energetic hardening terms, respectively. In Lebensohn et al. (2012) local EVP-FFT implementation only dissipative hardening needed to be accounted for. For this, the flow strength was updated implicitly within the polarization loop, such that the value of $g^{(\beta)}$ at time $(t + \Delta t)$ was re-calculated at the end of each iteration as:

$$g^{(\beta)} = g^{(\beta),t} + H_0 \sum_\alpha |\dot{\gamma}^{(\beta)}| \, \Delta t$$

(33)

In the present non-local implementation, however, the back-stress associated with energetic hardening is not updated inside the polarization loop, because such implicit update introduces instability in the numerical procedure. Instead, the back-stress values corresponding to time step t are used throughout the polarization loop corresponding to time $(t + \Delta t)$, and updated according to:

ARTICLE IN PRESS

10   R.A. Lebensohn, A. Needleman / J. Mech. Phys. Solids ∎ (∎∎∎∎) ∎∎∎–∎∎∎
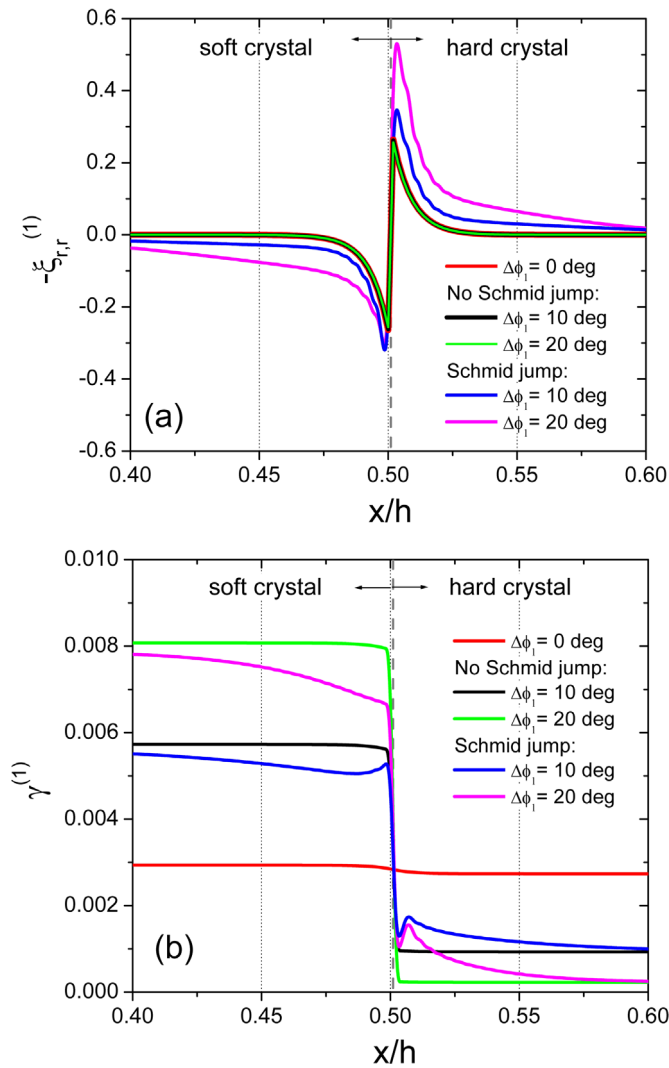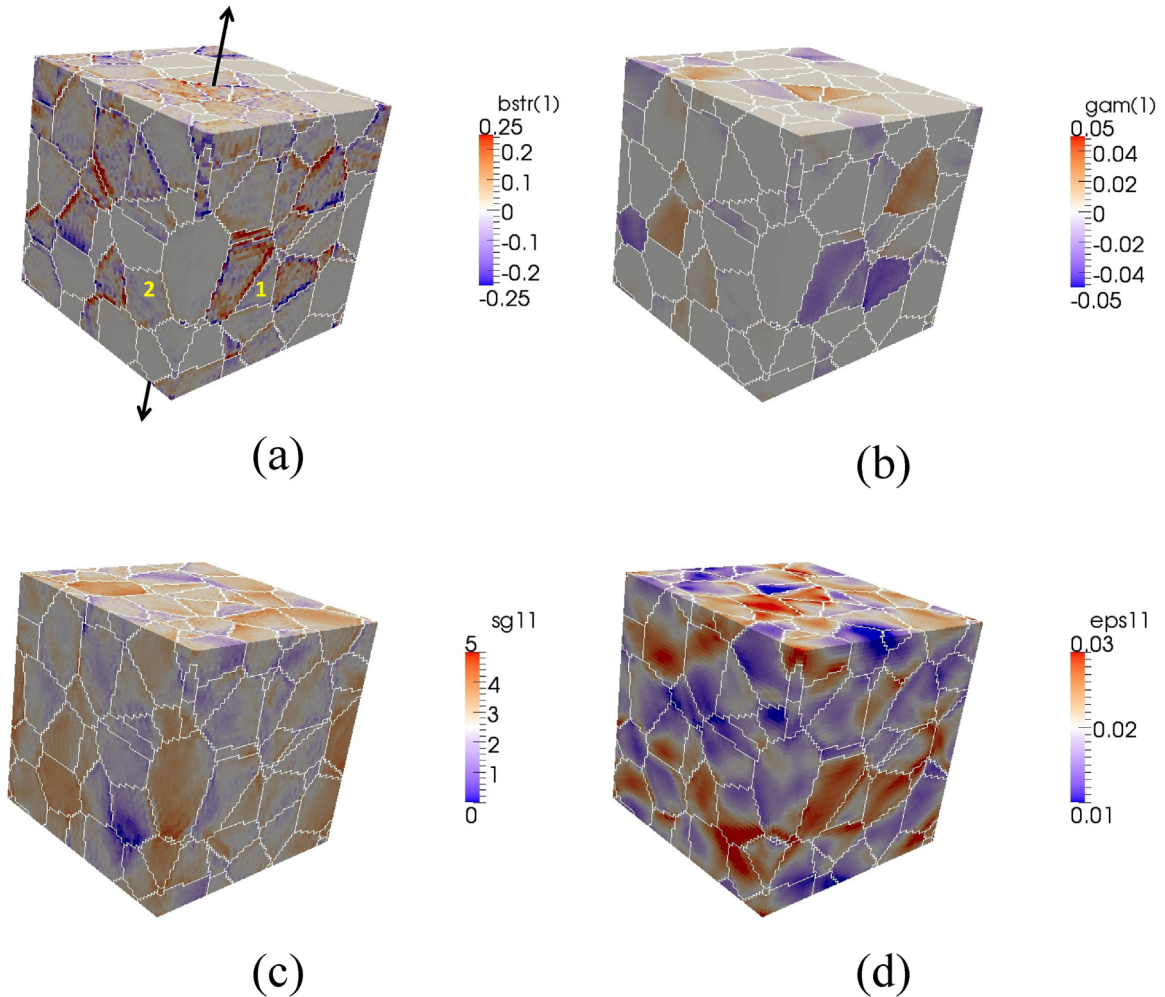

Fig. 6. Influence of crystal lattice misorientation. (a) Back-stress and (b) slip fields in the region near the interface, for active slip system #1 after 1% strain, for $d/\ell = 1$ and different values lattice misorientation between crystals, predicted with and without consideration of Schmid tensor jumps at the interface.
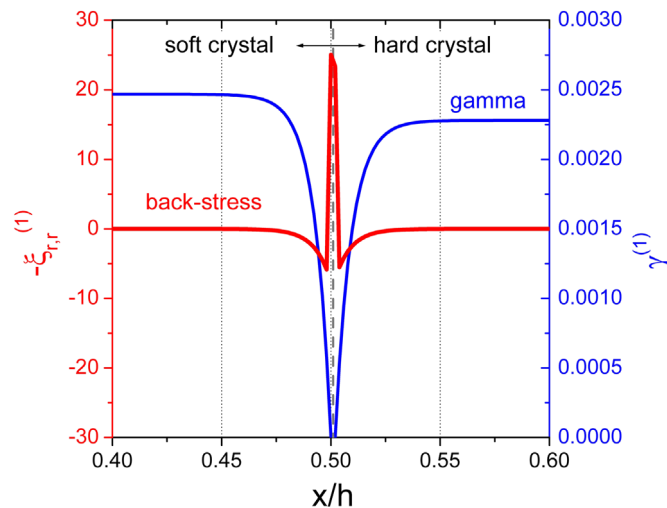
Fig. 7. Back-stress and slip fields near the interface for active slip #1 after 1% strain, for $d/\ell = 1$, in the micro-clamped interface case.

ARTICLE IN PRESS

R.A. Lebensohn, A. Needleman / J. Mech. Phys. Solids ∎ (∎∎∎∎) ∎∎∎–∎∎∎   11
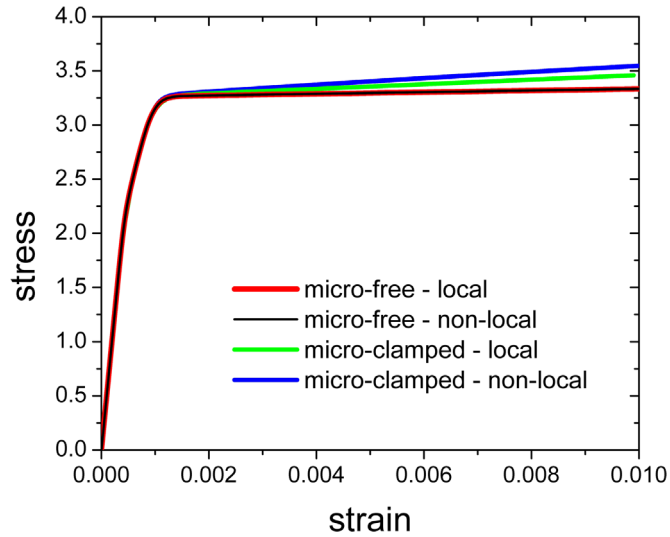
Fig. 8. Local vs. non-local predictions ($d/\ell = 1$) of the effective stress–strain response of the bicrystal, in the micro-free and micro-clamped interface cases.

Fig. 9. Micromechanical fields predicted by the non-local theory ($d/\ell = 1$) for the 3-D fcc polycrystal with 100 grains deformed 2% strain in uniaxial tension under micro-free conditions at grain boundaries. (a) Back-stress and (b) slip fields for active slip system #1; (c) longitudinal stress and (d) longitudinal strain fields.

ARTICLE IN PRESS

12   R.A. Lebensohn, A. Needleman / J. Mech. Phys. Solids ∎ (∎∎∎∎) ∎∎∎–∎∎∎

$$-\xi_{r,r}^{(\beta)} = -\xi_{r,r}^{(\beta),t} + \left(-\dot{\xi}_{r,r}^{(\beta)} \right) \Delta t \tag{34}$$

where $-\dot{\xi}_{r,r}^{(\beta)}$ is calculated using Eqs. (24) or (25), using the converged values of the slip rates $\dot{\gamma}^{(\beta)}$ coming out the polarization loop. These slip rates are used to calculate the plastic distortion rate and, in turn, its derivatives by means of Eqs. (26) or (31). This explicit update of the energetic hardening contribution requires the adoption of a sufficiently small time step to avoid numerical instability as the simulation advances in time. For the materials and applied boundary conditions studied here, the typical time step was 10^{-5} s.

4. Results

We illustrate here the proposed FFT-based non-local polycrystal plasticity numerical implementation with applications to: 1) bicrystals, by means of which we demonstrate the numerical stability of the proposed scheme, and conduct para-metric studies highlighting the influence of different numerical and constitutive parameters on the predictions of the non-local model, and 2) polycrystals, which allows us to exemplify the robustness and efficiency of the present numerical scheme to solve large 3-D problems.

4.1. Bicrystal

The bicrystal configuration adopted here to assess the proposed formulation consists of a periodic unit cell made of two fcc single crystal laminates of the same volume fraction. The crystals are infinitely extended along the y-and z-directions and they are separated by straight interfaces normal to x-direction at $x = 0$, $h/2$, h, $\cdots$, etc., which determines a grain size $d = h/2$. Note that this configuration renders the problem one-dimensional. Unless otherwise noted, the axes of both crystals are aligned with sample axes, in which case the use of Eq. (24) to calculate back-stresses suffices, and the micro-free boundary condition, $q^{(\beta)} = 0$, is adopted at grain boundaries. Heterogeneity is introduced in the plastic properties by spe-cifying two different initial values of the flow strength $\pi_0^s = \pi_0 = 1$ and $\pi_0^h = C \times \pi_0^s = C$, where s and h indicate the plastically soft and hard crystals, respectively, and C is the contrast ratio between the initial flow strengths of both crystals. Both crystals have the same isotropic elastic properties. We adopt here the same values used by Bittencourt et al. (2003), i.e. a Poisson's ratio $\nu = 0.33$ and a shear modulus relative to the value of the initial flow strength $\mu = 526 \times \pi_0/0.309 = 1702$. A uniaxial stress state along x is prescribed, up to a total longitudinal strain of 1%. The imposed value of the longitudinal component of the strain rate is 1 s^{-1}. The symmetry of the loading with respect to the crystals' orientation determines that 8 out 12 (111) < 110 > slip systems are equally activated. The laminate geometry determines that some strain components and the complementary stress components are uniform throughout the unit cell. Moreover, the local plasticity theory predicts that the 8 active slip fields $\gamma^{(\beta)}(\mathbf{x})$ are uniform within each crystal, with the amplitude of the jump across the interface being determined by the contrast in flow strength. This implies that the non-local theory should predict a pro-gressive build-up of back-stress fields near the interface.

First, in order to study the numerical stability of the back-stress calculation, which is a pre-requisite for a sound non-local theory implementation, we consider the case in which the back-stress is calculated using (Eqs. (24) and 34), but not used in
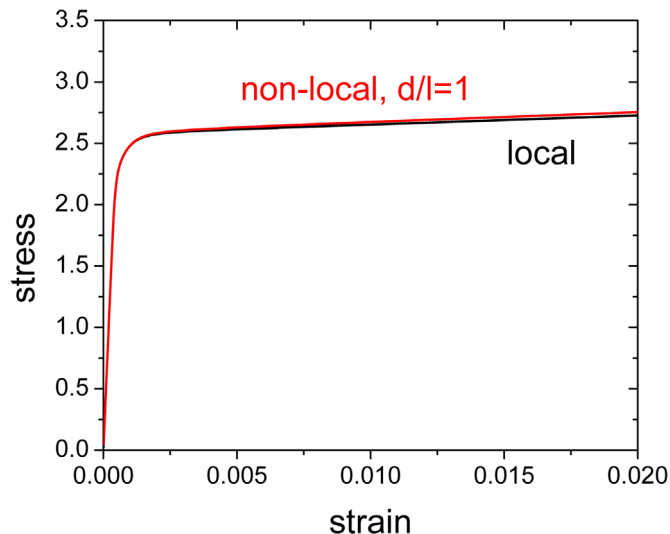

Fig. 10. Effective stress–strain response predicted by the local and non-local theories ($d/\ell = 1$) for the 3-D fcc polycrystal with 100 grains deformed 2% strain in uniaxial tension under micro-free conditions at grain boundaries.

ARTICLE IN PRESS

R.A. Lebensohn, A. Needleman / J. Mech. Phys. Solids ∎ (∎∎∎∎) ∎∎∎–∎∎∎　　　　13

(a)

(b)
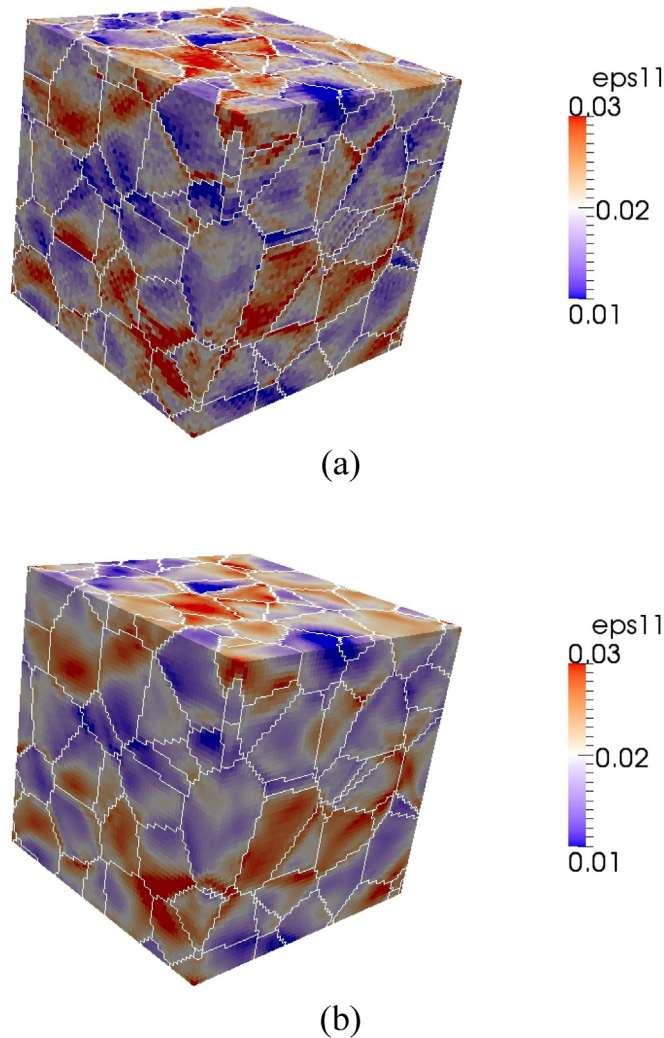
Fig. 11. Longitudinal strain field predicted by the (a) local vs (b) non-local theory ($d/\ell = 1$) for the 3-D fcc polycrystal with 100 grains, deformed 2% strain in uniaxial tension under micro-free conditions at grain boundaries.

the constitutive equation, rendering the predictions local. Fig. 1 shows a zoom near the interface at $x = h/2$ of the slip and back-stress fields of one out of eight active slip systems (identified as #1) after 1% strain. As expected from a local plasticity prediction, the slip field is uniform inside each crystal, with a sharp jump across the interface (note that the symbols correspond to the position of the Fourier points at which the fields are evaluated). As a consequence, $-\xi_{r,r'}^{(\beta)}(\mathbf{x})$ should be non-vanishing only at the two Fourier points immediately adjacent to the interface on both sides, and zero elsewhere. This is indeed the prediction obtained by means of DFT ((Eqs. (26), 27)). Instead, the use of CFT ((Eqs. (28)–30)) results in a solution with spurious oscillations extending away from the interface.

The bicrystal configuration is next used to assess how different numerical and constitutive parameters affect the non-local predictions. Fig. 2 shows the influence of the material length-scale. All cases correspond to C=2, $H_0^i = \pi_0^i$, $i = s$ & h, and a discretization specified by $N_1 = 512$. Fig. 2a and b shows a zoom near the interface of the back-stress and slip fields, respectively, corresponding to active slip system #1 after 1% strain, for different values of the ratio of grain size to material length, d/ℓ. The first observation, which also applies to all the subsequent non-local calculations is that, in contrast with the sharp slip and back-stress field jumps obtained with the local model shown in Fig. 1, the non-local theory predicts the formation of a boundary layer region in which the slip fields smoothly vary between the two different uniform values in the bulk of each laminate, and back-stress peaks with much smaller intensity (compare the 0.2–0.3 peaks in the non-local cases vs. values of the order of 10 in the local calculation) on both sides of the interface, showing a smooth decay to zero as the distance from the interface increases. The reason for these differences is that the use of the back-stress in the constitutive equation tends to make regions of the soft crystal near the interface harder to deform. This produces smoother slip fields, slowing down the build-up of back-stresses near the interface. Interestingly, the positive values of $-\xi_{sr,r'}^{(\beta)}$ on the hard side of the interface act as a forward-stress, producing the opposite effect.

ARTICLE IN PRESS

14   *R.A. Lebensohn, A. Needleman / J. Mech. Phys. Solids ∎ (∎∎∎∎) ∎∎∎–∎∎∎*
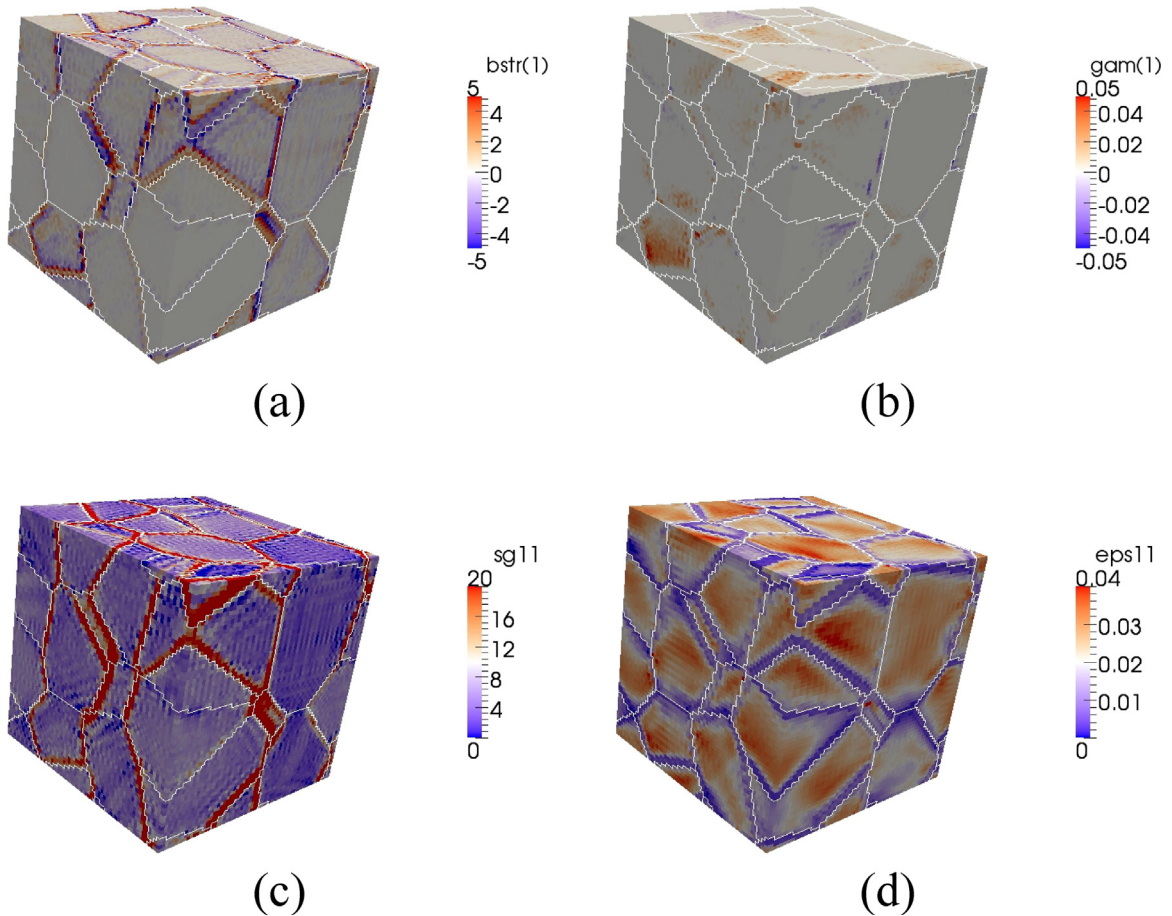
Fig. 12. Micromechanical fields predicted by the non-local theory ($d/\ell = 1$) for the 3-D fcc polycrystal with 27 grains deformed 2% strain in uniaxial tension, imposing micro-clamped conditions at grain boundaries. (a) Back-stress and (b) slip fields for active slip system #1; (c) longitudinal stress and (d) longitudinal strain fields.

Specifically concerning the effect of the material length-scale, the thickness of the boundary layer increases as d/ℓ decreases, that is when the material length-scale becomes comparable with the grain size, in which case the size effect becomes stronger. As for the back-stress field, the positive and negative peak values at both sides of the interface, as well as the thickness of the regions in which the back-stress adopts non-negligible values, increase as d/ℓ decrease, consistent with a more pronounce size effect at smaller material length-scales.

Fig. 3 shows the effect of the discretization adopted for the FFT-based calculation. All cases correspond to $d/\ell = 1$, C=2 and $H_0^i = \pi_0^i$. Fig. 3a and b zoom near the interface, showing the back-stress and slip fields, respectively, for active slip #1 after 1% strain, for different discretizations. Note that in this case the interface was not plotted, since its position (i.e. the mid-point between the two adjacent Fourier points belonging to different crystals) varies slightly with the discretization adopted. We observe that, while in the case of the slip field the predictions are practically independent of the resolution, the back-stress peaks increase at higher resolutions. This is due to the fact that, as resolution increases, the two Fourier points adjacent to the interface at which the peak back-stresses occur become closer to the interface, indicating that the back-stress field itself also remains, for the most part, unchanged with increasing resolution. Moreover, it is apparent that the peak value increase slows down as the resolution increases.

Fig. 4 shows how the contrast between plastic properties of the crystals affects the predictions. All cases correspond to $d/\ell = 1$, $H_0^i = \pi_0^i$ and a 512 discretization. Fig. 4a and b show the back-stress and slip fields, respectively, in the region near the interface, corresponding to active slip #1 after 1% strain, for contrasts C=2, 5 and 10, while Fig. 4c and d correspond to the higher contrasts C=20 and 50. Note the different scales required, as compared with the previous Figs. 2 and 3, corresponding C=2. It is observed that the slip in the hard crystal decreases as contrast increases. The back-stress peak values increase with increasing contrast, but, for the lower contrasts, the thickness of the region in which the back-stress adopts non-negligible values remains unchanged. The hard crystal remains almost fully elastic at the highest contrast C=50. For this high contrast, the back-stress becomes asymmetric with a higher peak value on the hard side of the interface. This can be understood in terms of a dislocation pile-up on the plastic side of the interface creating a forward-stress on the hard crystal that is accommodated elastically. Interestingly, this forward-stress decreases faster into the hard crystal than in the

ARTICLE IN PRESS

R.A. Lebensohn, A. Needleman / J. Mech. Phys. Solids ∎ (∎∎∎∎) ∎∎∎–∎∎∎   15
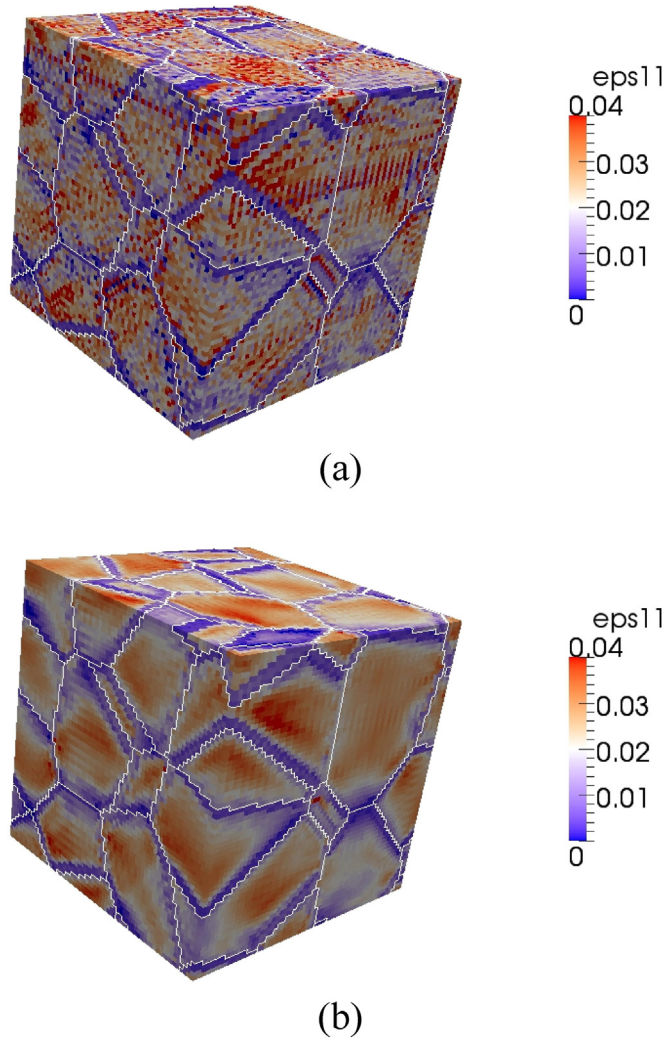
Fig. 13. Longitudinal strain field predicted by the (a) local vs (b) non-local theory ($d/\ell = 1$) for the 3-D fcc polycrystal with 27 grains deformed 2% strain in uniaxial tension, imposing micro-clamped conditions at grain boundaries.

lower contrast cases in which the hard crystal shows some level of plastification.

Fig. 5 shows the effect of dissipative hardening on the energetic hardening. All cases correspond to $d/\ell = 1$, C=2, and a 512 discretization. Fig. 5a and b shows the back-stress and slip fields, respectively, in the region near the interface, corresponding to active slip #1 after 1% strain, for different values of the dissipative hardening parameter H_0. We compare predictions for the dissipative hardening imposed in all previous cases, $H_0^i = 1 \times \pi_0^i$, to the cases with no dissipative hardening, $H_0^i = 0$, and for a dissipative hardening ten times higher, $H_0^i = 10 \times \pi_0^i$. We observe that in the cases with $H_0^i = 0$ and $H_0^i = 1 \times \pi_0^i$ both the back-stress and the slip fields are almost indistinguishable, while for the highest value of the dissipative hardening parameter, the back-stress peaks slightly increase while the slip in both crystals slightly decreases. The mild influence of the dissipative hardening on the extent of the boundary layer, at least for this bicrystal configuration, shown in Fig. 5 differs from the FE results of Bittencourt et al. (2003) where, for the case of simple shear of a constrained crystal, there was a strong effect of the value of dissipative hardening parameter on the shape of the boundary layer.

Next, the bicrystal configuration is adapted to study the effect of crystal lattice misorientation. We consider a similar unit cell as in the previous cases, but with the crystal lattices of the laminates rotated $\pm\varphi_1/2$ with respect to the z-axis, determining a twist grain boundary with misorientation $\Delta\varphi_1$ and, consequently, a jump of the Schmid tensor fields across the interface. Fig. 6 corresponds to $d/\ell = 1$, C=2, $H_0^i = 1 \times \pi_0^i$, for a 512 discretization. Fig. 6a and b shows the back-stress and slip fields, respectively, in the region near the interface, corresponding to active slip #1 after 1% strain, for misorientations $\Delta\varphi_1 = 0°$, 10°, 20°, predicted by either neglecting (Eq. (24)) or accounting for (Eq. (25)) Schmid tensor jumps. In the case with no misorientation there is obviously no difference between using of both expressions. As misorientation increases, the slips in the bulk of both crystals become increasingly different. However, Eq. (24) predicts practically no differences in back-stress field profiles. On the other hand, the consideration of Schmid tensor jumps gives higher peaks, especially in the hard

ARTICLE IN PRESS

16   *R.A. Lebensohn, A. Needleman / J. Mech. Phys. Solids ∎ (∎∎∎∎) ∎∎∎–∎∎∎*
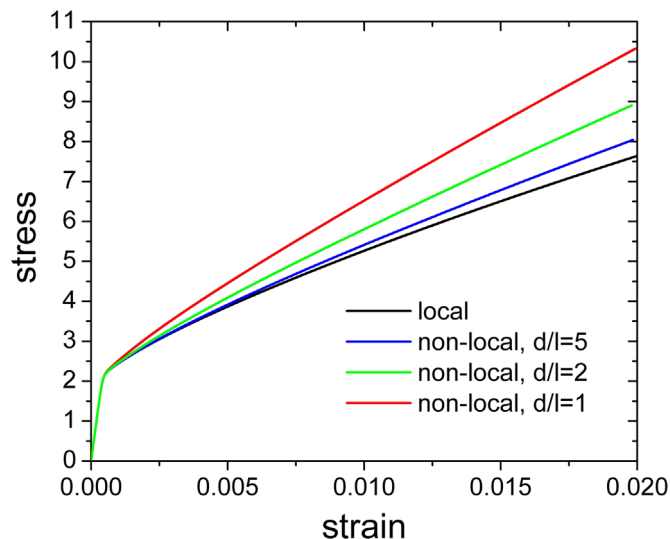
Fig. 14. Effective stress–strain response predicted by the local formulation and the non-local theory for different d/ℓ ratios, under micro-clamped conditions at grain boundaries. Case of the 3-D fcc polycrystal with 27 grains deformed up to 2% strain in uniaxial tension.

crystal, and more extended back-stress fields, as misorientation increases. The assumption of ideal slip transmissibility across grain boundaries introduces an underestimation of non-local effects that increases with misorientation.

In the examples presented so far, while the presence of the grain boundary alters slip due to the different plastic properties of the crystals on both sides of the interface, slip activity does not vanish in general at the grain boundary, like it does under the micro-clamped boundary condition, $\gamma^{(\beta)} = 0$, which is known to be responsible for the most pronounced size effects (Bittencourt et al., 2003). In the context of the present approach, we can force the micro-clamped condition by harden the local properties of the crystals at the interface. The bicrystal configuration is therefore adapted to enforce the micro-clamped condition at the grain boundary by assigning pure elastic behavior (in practice, assigning sufficiently high flow strength) to the two grid points adjacent to the interface. Fig. 7 shows the back-stress and slip fields near the interface for active slip #1 after 1% strain, for $d/\ell = 1$, C=2, $H_0^i = 1 \times \pi_0^i$, and a 512 discretization, for the micro-clamped interface condition. By construction, the slip vanishes at the interface and the back-stress peaks are one order magnitude higher than in the micro-free interface case. The negative of the micro-force is now a proper back-stress on both sides of the interface (previously $-\xi_{r,r}^{(\beta)}$ was acting as a forward-stress in the hard crystal). The micro-clamped approximation also gives a noticeable size effect on the effective behavior. Fig. 8 shows the local and non-local predictions for the effective stress–strain response of the bicrystal, in the micro-free and micro-clamped interface cases. The size effect obtained in the latter case is absent in the former. Considering the material length-scale ($d/\ell = 1$), the effect is still relatively minor, which can be attributed to a low density of grain boundaries, i.e. only one interface per unit cell. The size effect on the effective stress–strain response for micro-clamped grain boundaries becomes much stronger in the 3-D polycrystal cases presented next.

4.2. Polycrystal

In this subsection we first present results of the non-local theory for micro-free interfaces, and compare them with corresponding local predictions for the case of a 3-D polycrystalline periodic unit cell discretized using a $64 \times 64 \times 64$ grid, consisting of 100 fcc grains generated by Voronoi tessellation. We then analyze the case of micro-clamped grain boundaries for another $64 \times 64 \times 64$ 3-D polycrystalline unit cell with 27 Voronoi grains. In all cases, the back-stress field is calculated using the approximation given by Eq. (24), i.e. neglecting the contribution of Schmid tensor jumps across grain boundaries. Accounting for the latter by application of Eq. (25) would require considering that the best aligned slip system across a grain boundary may correspond to a different identification number $\beta = 1, 12$, requiring a refinement in the bookkeeping aspects of algorithm that has not been implemented yet.

Fig. 9 shows the micromechanical fields predicted by the non-local model for $d/\ell = 1$ (where the grain size and the unit cell size are related by $d = h/\sqrt[3]{100} = h/4.642$), after 2% strain in uniaxial tension along the x-direction, indicated by the arrows in Fig. 9a. Plots correspond to the back-stress and slip fields for active slip system #1, and to the longitudinal stress (σ_{11}) and strain (ε_{11}) fields. The adopted elastic and plastic properties are the same as in the previous bicrystal cases given by the following values, normalized with respect to the initial plastic flow strength: $\mu = 1702$, $\nu = 0.33$, and $\pi_0 = H_0 = 1$. We observe that the grains in which the back-stress associated with a given slip system has high positive or negative values are those where the slip on that system is favored, and their immediate neighbors. This is the case, for example, of the cluster of 3 grains marked with "1" in Fig. 9a, showing relatively high negative slip activity, on system #1. In particular, large back-

ARTICLE IN PRESS

R.A. Lebensohn, A. Needleman / J. Mech. Phys. Solids ∎ (∎∎∎∎) ∎∎∎–∎∎∎   17

stress values tend to decorate regions near grain boundaries, where slip gradients are prone to develop due to dislocation pile-ups forming against those grain boundaries. The sign of the non-local constitutive parameter $-\xi_{r,r'}^{(\beta)}$ is mainly positive, acting as a true back-stress in this case of negative slips, although regions near grain boundaries with negative values are also found, indicating complex effects of grain interaction on the slip fields and their gradients. Despite of the aforementioned predominance of large back-stresses near grain boundaries, it is also apparent the development of significant back-stresses in the bulk of some grains, indicating the formation of intragranular microstructure. Some of these intragranular regions of high GND content appear to have developed from triple junctions, as continuation of a highly strained grain boundary formed by the two other neighbor grains forming the triple junction. This is consistent with the CPFE results of Kanjarla et al. (2011). Another region of interest is the one marked with "2" in Fig. 9a, corresponding to a soft grain with very low longitudinal stress values and crossed by a transgranular high strain band. The grain to the left of the soft grain shows a moderate positive slip activity and a significant forward-stress, i.e. $-\xi_{r,r'}^{(\beta)}$ also positive, which favors slip and therefore transgranular strain localization.

Next, we present and analyze the differences between local and non-local predictions for the same polycrystalline unit cell deformed under the same conditions. Fig. 10 shows the effective stress–strain curves predicted by both theories. A very mild increase of the stress response is obtained with the non-local formulation with micro-free interfaces. Regarding the micromechanical fields, Fig. 11 shows the longitudinal strain field predicted by both theories at 2% strain. Besides some noticeable differences in the strain distribution that are clearly related to the consideration of non-local effects, the non-local predictions are also significantly smoother. Specifically, the undesirable checkerboard appearance of the strain field predicted with the local model is absent in non-local model results. This smoothing effect is also attributed to the consideration of strain gradients affecting the single crystal behavior.

The effect of imposing micro-clamped conditions at grain boundaries is analyzed next. For this, a 3-D polycrystalline unit cell with 27 grains was constructed as follows (Lebensohn et al., 2007). We first applied the standard discrete Voronoi algorithm, consisting in randomly distributing 27 grain nuclei with random crystallographic orientations in the cubic unit cell and assigning each Fourier point (FP) to its nearest nucleus, accounting for periodic boundary conditions across the unit cell limits. Next we identified the FPs with at least on first neighbor FP belonging to a different grain and assigned them hard local properties, i.e. pure elastic behavior, achieved by imposing sufficiently high flow strength.

Fig. 12 shows the micromechanical fields predicted by the non-local theory for $d/\ell = 1$ (with $d = h/\sqrt[3]{27} = h/3$) using the above procedure to force micro-clamped conditions at grain boundaries, after 2% strain in uniaxial tension. We observe that the back-stress continues being concentrated at grain boundaries with peak values that are more than one order of magnitude higher than in the soft grain boundaries case. The slip fields are more heterogeneous, adopting relatively high values in the bulk of some well oriented grains that tend to vanish in the proximities of grain boundaries. Consistent with the enforced micro-clamped condition, the stresses are high and the strains are low near interfaces.

The comparison between local and non-local predictions in this case of hard interfaces is illustrative of the numerical benefits of using strain-gradient plasticity. Fig. 13 shows the longitudinal strain field predicted by the local and non-local theories imposing micro-clamped conditions at grain boundaries at 2% strain in uniaxial tension. The local predictions display a severe checkerboard appearance that is smoothed out when non-local effects are considered.

Fig. 14 shows the effective stress-strain curves predicted by the local formulation and the non-local theory for different d/ℓ ratios, under micro-clamped conditions at grain boundaries. For this configuration with higher density of interfaces, the size effect on the effective stress-strain response for micro-clamped grain boundaries is significant.

5. Remarks

1) The comparison of Fig. 1, between the back-stress calculation using CFT and DFT illustrates the need of the latter for a sound spectral implementation of this particular non-local model and, for that matter, of any other formulation requiring the calculation of higher order derivatives. This is especially the case when these derivatives are subsequently used in the determination of parameters affecting the constitutive response at local level. Moreover, the use of a DFT-based algorithm to calculate derivatives in Fourier space has also been instrumental in improving the accuracy of FFT-based formulations in general, as an alternative to the CFT-based expression given by Eq. (23) to calculate the Green operator in Fourier space $\hat{\Gamma}_{ijkl}^{o}(\mathbf{k})$, which itself involves second derivatives (Willot and Pellegrini, 2008; Willot, 2015).

2) The approximate expression to calculate the back-stress field given by Eq. (24), which neglects spatial variations of the Schmid tensors, is strictly valid in most of the bicrystal cases of Section 4.1, due to the purposely chosen perfect alignment of both crystals. This, however, is in general not the case for polycrystals (even for aggregates of cubic crystals with a large number of symmetrically equivalent slip systems available), in which a more accurate estimation of the back-stress field would require the evaluation of Eq. (25). However, performing this computation in a general polycrystalline setting turns out to be a challenging problem, given the fact that the best aligned slip system across a grain boundary may correspond to a different identification number $\beta = 1,12$. Coming up with viable ways to solve this numerical issue is especially relevant in connection with the study of the effect of slip transmissibility across grain boundaries. Efforts in this direction are underway.

3) Although we have not conducted a one-to-one comparison between a non-local CPFE calculation and the present

ARTICLE IN PRESS

18   *R.A. Lebensohn, A. Needleman / J. Mech. Phys. Solids ∎ (∎∎∎∎) ∎∎∎–∎∎∎*

numerical scheme, and our focus has not been on optimizing the non-local EVP-FFT code, but on establishing the algorithmic requirements for a sound and numerically stable calculation, we can provide some measure of the performance of our implementation. For example, in the 3-D fcc polycrystal case above, discretized by means of a $64 \times 64 \times 64$ grid, i.e. involving around 250,000 degrees of freedom, the computing time on a single processor with standard speed to resolve the micromechanical fields at given time step is of the order of 20 s (this computing time varies because the number of iterations for convergence of the polarization varies between time increments). Therefore, for a time increment of 10^{-5} s, the time to compute a strain of 1% is around 5 h. Of course, a parallel implementation would significantly decrease the computation time.

4) Our analyses have been based on a non-local crystal constitutive relation where size effects are due to plastic strain gradients. Hence, as seen for example in Fig. 14, there is no size effect on initial yield. However, our results indicate that there would be a size effect on a flow strength defined by an offset plastic strain. The extent to which accounting for size-dependent hardening in a heterogeneous grain microstructure is sufficient to account for the observed size effect on flow strength remains to be determined.

6. Conclusions

The first implementation of a non-local polycrystal plasticity theory using the FFT-based formulation of Moulinec and Suquet (1994, 1998) was presented. Specifically, Gurtin (2002) non-local theory was incorporated in the EVP-FFT algorithm of Lebensohn et al. (2012). Critical numerical issues were identified and fixed. The proposed methodology for an accurate estimation of higher order derivatives of micromechanical fields, required for feedback into the single crystal constitutive relations, should be applicable to the numerical implementation of other non-local theories in the context of spectral formulations. A simple laminate made of two crystals with different plastic properties was used to assess the soundness and numerical stability of the proposed algorithm. Parametric studies involving variations of length-scale, adopted discretization, mechanical contrast, and dissipative hardening were conducted, showing expected trends. For bicrystals with lattice misorientation, the approximation involved in the back-stress calculation neglecting spatial derivatives of the Schmid tensor was assessed and it may become significant at large misorientations. Two extreme types of interface conditions, corresponding to either allowing slip at grain boundaries as determined by crystallography and the applied loading, or completely blocking slip, were compared. The former free slip condition at grain boundaries produced a very minor effect of the material length scale on the effective response, while the latter micro-clamped condition gave rise to a much pronounced size effect. The actual behavior of grain boundaries is expected to fall between these extreme regimes. Our formulation was applied next to 3-D polycrystals, illustrating the possibilities offered by the proposed scheme to accurately solve relatively large 3-D non-local crystal plasticity problems in reasonable computing times. Specifically in terms of variations of model parameters, these 3-D computations showed similar trends as previously obtained in the bicrystal cases. Moreover, from a strictly numerical point of view, the 3-D examples illustrated the beneficial effect of considering strain gradients to avoid spurious oscillations of the predicted micromechanical fields.

Our results indicate that the developed FFT method provides a promising basis for the accurate and efficient calculation of polycrystal response accounting for grain size effects due to slip gradients. However, in order to turn this formulation into a predictive tool several further developments are needed, in particular: (i) an accurate and efficient method to account for the grain-to-grain variation of the Schmid tensor needs to be developed: (ii) the finite geometry changes leading to slip system reorientations need to be accounted for; and (iii) more detailed models of grain boundary slip blocking and slip transmission need to be developed. The development of such a framework would provide a tool for size-dependent grain morphology design.

References

Acharya, A., Bassani, J.L., 2000. Incompatibility and crystal plasticity. J. Mech. Phys. Solids 48, 1565–1595.
Anglin, B.S., Lebensohn, R.A., Rollett, A.D., 2014. Validation of a numerical method based on fast Fourier transforms for heterogeneous thermoelastic materials by comparison with analytical solutions. Comput. Mat. Sci. 87, 209–217.
Ashby, M.F., 1970. The deformation of plastically non-homogeneous materials. Philos. Mag. 21, 399–424.
Balint, D.S., Deshpande, V.S., Needleman, A., Van der Giessen, E., 2008. Discrete dislocation plasticity analysis of the Hall-Petch effect. Int. J. Plast. 24, 2149–2172.
Berbenni, S., Taupin, V., Djaka, K.S., Fressengeas, C., 2014. A numerical spectral approach for solving elasto-static field dislocation and g-disclination mechanics. Int. J. Solids Struct. 51 (23–24), 4157–4175.
Biner, S.B., Morris, J.R., 2003. The effects of grain size and dislocation source density on the strengthening behaviour of polycrystals: a two-dimensional discrete dislocation simulation. Phil. Mag. 83, 3677–3690.

ARTICLE IN PRESS

R.A. Lebensohn, A. Needleman / J. Mech. Phys. Solids ∎ (∎∎∎∎) ∎∎∎–∎∎∎   19

Bittencourt, E., 2014. Dynamic explicit solution for higher-order crystal plasticity theories. Int. J. Plast. 53, 1–16.
Bittencourt, E., Needleman, A., Van der Giessen, E., Gurtin, M.E., 2003. A comparison of nonlocal continuum and discrete dislocation plasticity predictions. J. Mech. Phys. Solids 51, 281–310.
Brenner, R., Lebensohn, R.A., Castelnau, O., 2009. Elastic anisotropy and yield surface estimates of polycrystals. Int. J. Solids Struct. 46, 3018–3026.
Cordero, N.M., Forest, S., Busso, E.P., Berbenni, S., Cherkaoui, M., 2012. Grain size effects on plastic strain and dislocation density tensor fields in metal polycrystals. Comput. Mater. Sci. 52, 7–13.
Counts, W.A., Braginsky, M.V., Battaile, C.C., Holm, E.A., 2008. Predicting the Hall-Petch effect in fcc metals using non-local crystal plasticity. Int. J. Plast. 24, 1243–1263.
Danas, K., Deshpande, V.S., Fleck, N.A., 2012. Compliant interfaces: a mechanism for relaxation of dislocation pile-ups in a sheared single crystal. Int. J. Plasticity 26, 1792–1805.
De Guzman, M.S., Neubauer, G., Flinn, P., Nix, W.D., 1993. The role of indentation depth on the measured hardness of materials. Mater. Res. Symp. Proc. 308, 613–618.
Dreyer, W., Müller, W.H., Olschewski, J., 1999. An approximate analytical 2D-solution for the stresses and strains in eigenstrained cubic materials. Acta Mech. 136, 171–192.
Eisenlohr, P., Diehl, M., Lebensohn, R.A., Roters., F., 2013. A spectral method solution to crystal elasto-viscoplasticity at finite strains. Int. J. Plast. 46, 37–53.
Eshelby, J.D., Frank, F.C., Nabarro, F.R.N., 1951. The equilibrium of line arrays of dislocations. Phil. Mag. 42, 351–364.
Fleck, N.A., Hutchinson, J.W., 1993. A phenomenological theory for strain gradient effects in plasticity. J. Mech. Phys. Solids 41, 1825–1857.
Fleck, N.A., Hutchinson, J.W., 1997. Strain gradient plasticity. Adv. Appl. Mech. 33, 295–361.
Fleck, N.A., Hutchinson, J.W., 2001. A reformulation of strain gradient plasticity. J. Mech. Phys. Solids 49, 2245–2271.
Fleck, N.A., Muller, G.M., Ashby, F., Hutchinson, J.W., 1994. Strain gradient plasticity: theory and experiment. Acta Metall. Mater. 42, 475–487.
Forest, S., 2008. Some links between Cosserat, strain gradient crystal plasticity and the statistical theory of dislocations. Phil. Mag. 88, 3549–3563.
Gao, H., Huang, Y., Nix, W.D., Hutchinson, J.W., 1999. Mechanism-based strain gradient plasticity—I. Theory. J. Mech. Phys. Solids 47, 1239–1263.
Greer, J.R., Oliver, W.C., Nix, W.D., 2005. Size dependence of mechanical properties of gold at the micron scale in the absence of strain gradients. Acta Mater. 53, 1821–1830.
Grennerat, F., Montagnat, M., Castelnau, O., Vacher, P., Moulinec, H., Suquet, P., Duval, P., 2012. Experimental characterization of the intragranular strain field in columnar ice during transient creep. Acta Mater. 60, 3655–3666.
Gurtin, M.E., 2000. On plasticity of crystals: free energy, microforces, plastic strain gradients. J. Mech. Phys. Solids 48, 989–1036.
Gurtin, M.E., 2002. A gradient theory of single-crystal viscoplasticity that accounts for geometrically necessary dislocations. J. Mech. Phys. Solids 50, 5–32.
Gurtin, M.E., Needleman, A., 2005. Boundary conditions in small-deformation, single-crystal plasticity that account for the Burgers vector. J. Mech. Phys. Solids 53, 1–31.
Hall, E.O., 1951. The deformation and ageing of mild steel: III. Discussion of results. Proc. Phys. Soc. B64, 747–753.
Hirth, J.P., Lothe, J., 1968. Theory of Dislocations. McGraw-Hill, New York.
Hwang, K.C., Guo, Y., Jiang, H., Huang, Y., Zhuang, Z., 2004. The finite deformation theory of Taylor-based nonlocal plasticity. Int. J. Plast. 20, 831–839.
Kanjarla, A.K., Delannay, L., Van Houtte, P., 2011. Finite element study of intragrain plastic heterogeneity near a triple junction. Met. Trans. 42A, 660–668.
Kuroda, M., 2015. A higher-order strain gradient plasticity theory with a corner-like effect. Int. J. Solids Struct. 58, 62–72.
Kuroda, M., Tvergaard, V., 2008. On the formulations of higher-order strain gradient crystal plasticity models. J. Mech. Phys. Solids 56, 1591–1608.
Lebensohn, R., Kanjarla, A., Eisenlohr, P., 2012. An elasto-viscoplastic formulation based on fast Fourier transforms for the prediction of micromechanical fields in polycrystalline materials. Int. J. Plasticity 32-33, 59–69.
Lebensohn, R.A., 2001. N-site modeling of a 3-D viscoplastic polycrystal using fast Fourier transform. Acta Mater. 49, 2723–2737.
Lebensohn, R.A., Bringa, E.M., Caro, A., 2007. A viscoplastic micromechanical model for the yield strength of nanocrystalline materials. Acta Mater. 55, 261–271.
Lebensohn, R.A., Brenner, R., Castelnau, O., Rollett, A.D., 2008. Orientation image-based micromechanical modelling of subgrain texture evolution in polycrystalline copper. Acta Mater. 56, 3914–3926.
Lebensohn, R.A., Montagnat, M., Mansuy, P., Duval, P., Meysonnier, J., Philip, A., 2009. Modeling viscoplastic behavior and heterogenous intracrystalline deformation of columnar ice polycrystals. Acta Mater. 57, 1405–1415.
Müller, W.H., 1998. Fourier transforms and their application to the formation of textures and changes of morphology in solids. In: IUTAM Symposium on Transformation Problems in Composite and Active Materials. Kluwer Academic Publishers, pp. 61–72.
Ma, Q., Clarke, D.R., 1995. Size-dependent hardness of silver single-crystals. J. Mater. Res. 10, 853–863.
Mayeur, J.R., McDowell, D.L., 2014. A comparison of Gurtin type and micropolar theories of generalized single crystal plasticity. Int. J. Plast. 57, 29–51.
Michel, J.C., Moulinec, H., Suquet, P., 2000. A computational method based on augmented Lagrangians and fast Fourier transforms for composites with high contrast Comput. Model Eng. Sci 1, 79–88.
Michel, J.C., Moulinec, H., Suquet, P., 2001. A computational scheme for linear and non-linear composites with arbitrary phase contrast. Int. J. Numer. Meth. Eng. 52, 139–158.
Moulinec, H., Suquet, P., 1994. A fast numerical method for computing the linear and nonlinear mechanical properties of composites. C. R. Acad. Sci. Paris II 318, 1417–1423.
Moulinec, H., Suquet, P., 1998. Numerical method for computing the overall response of nonlinear composites with complex microstructure. Comput. Methods Appl. Mech. Eng. 157, 69–94.
Niordson, C.F., Kysar, J.W., 2014. Computational strain gradient crystal plasticity. J. Mech. Phys. Solids 62, 31–47.
Nye, J.F., 1953. Some geometrical relations in dislocated solids. Acta Metall. 1, 153–162.
Petch, N.J., 1953. The cleavage strength of polycrystals. J. Iron Steel Inst. 174, 25–28.
Quek, S.S., Wu, Z., Zhang, Y.W., Srolovitz, D.J., 2014. Polycrystal deformation in a discrete dislocation dynamics framework. Acta Mater. 75, 92–105.
Stölken, J.S., Evans, A.G., 1998. A microbend test method for measuring the plasticity length scale. Acta Mater. 46, 5109–5115.
Uchic, M.D., Dimiduk, D.M., Florando, J.N., Nix, W.D., 2004. Sample dimensions influence strength and crystal plasticity. Science 305, 986–989.
Willot, F., 2015. Fourier-based schemes for computing the mechanical response of composites with accurate local fields. Comptes Rendus Mecanique 343, 232–245.
Willot, F., Pellegrini, Y.P., 2008. Fast Fourier transform computations and build-up of plastic deformation in 2D, elastic–perfectly plastic, pixelwise-disordered porous media. In: Continuum Models and Discrete Systems, CMDS11, D. Jeulin, S. Forest (Eds.), École des Mines, Paris, pp. 443–449.